New formulation of the Fourier modal method for crossed surface-relief gratings

Lifeng Li

Optical Sciences Center, University of Arizona, Tucson, Arizona 85721

Received February 24, 1997; accepted March 31, 1997

A new formulation of the Fourier modal method (FMM) that applies the correct rules of Fourier factorization for crossed surface-relief gratings is presented. The new formulation adopts a general nonrectangular Cartesian coordinate system, which gives the FMM greater generality and in some cases the ability to save computer memory and computation time. By numerical examples, the new FMM is shown to converge much faster than the old FMM. In particular, the FMM is used to produce well-converged numerical results for metallic crossed gratings. In addition, two matrix truncation schemes, the parallelogramic truncation and a new circular truncation, are considered. Numerical experiments show that the former is superior. © 1997 Optical Society of America [S0740-3232(97)02610-0]

1. INTRODUCTION

A crossed grating is a grating that is periodic in two noncollinear directions. In the literature synonyms such as bigratings and two-dimensional gratings are also used. These synonyms are less preferable because the term bigrating has been used by some authors to mean a two-grating assembly with collinear grating vectors, and two-dimensional gratings are sometimes referred to as three-dimensional gratings.

Crossed gratings have many applications. For example, they can be used as laser beam fan-out elements, solar energy absorbers, antireflection surfaces, artificial graded-index materials, artificial anisotropic materials, etc. In general, the analysis of these elements requires electromagnetic theory and complicated computer programs.

To date, many rigorous numerical methods exist for modeling crossed gratings. A partial list includes the differential method,[1–3] the coordinate transformation method,[4–7] the integral method,[8] the Fourier modal method,[9,10] the Rayleigh method,[11] and the boundary variation method.[12,13] However, all of these methods tend to be memory hungry and time consuming. After a simple back-of-the-envelope calculation to estimate how many diffraction orders must be retained in the computation for a typical crossed grating problem, one can quickly realize that even some of the most modern desktop computers may not have enough dynamic memory and that one has to wait for minutes or hours to obtain the results of a (fixed) grating configuration. Hence searching for innovative numerical methods for crossed gratings or improving the convergence speed of existing methods is of great practical significance.

This paper is aimed at improving the convergence speed of the Fourier modal method (FMM) [also known as the coupled-wave method and the modal method by Fourier expansion (MMFE)]. It differs from the previous FMM analysis[9,10] in three respects:

1. The FMM for crossed gratings is reformulated by using the correct rules for Fourier factoring products that contain discontinuous functions.[14] It was shown recently[15,16] that the newly formulated one-dimensional FMM with use of the correct factorization rules converged much faster than the old FMM. Many researchers' attention naturally turned to the two-dimensional FMM, hoping to achieve a similar improvement. The application of the results of Refs. 14–16 to crossed gratings turns out to be not so straightforward. The work reported here is a successful attempt.

2. The previous FMM for crossed gratings, and in fact all methods mentioned above with one recent exception,[7] used a rectangular Cartesian coordinate system in the plane of the grating, even when the grating did not possess two orthogonal periodic directions. In this paper a Cartesian coordinate system is used, whose two axes in the grating plane follow two periodic directions of the grating, which are in general not orthogonal to each other. The use of such a coordinate system not only makes the theoretical presentation more elegant and the theory itself more general but in some cases also reduces memory requirement and computation time.

3. When carrying out numerical computations, all authors of crossed gratings have chosen to retain diffraction orders that lie in a parallelogramic area centered around the zeroth diffraction order in the two-dimensional Fourier space. In this paper the convergence characteristics of two truncation schemes, one using a parallelogramic area and the other using a circular area, with both centered around the origin of the Fourier space, are compared.

In conducting this research, I have followed one principle: keeping in mind the high demand of the crossed grating problem on computer resources, to make every possible effort to reduce memory consumption and to increase convergence speed. Owing to limitations in time and in the computing resources available to me, the results presented here on the convergence characteristics of the new FMM are preliminary.

Since a nonrectangular Cartesian coordinate system is used in this paper, it is convenient to use tensor notation

0740-3232/97/1002758-10$10.00 © 1997 Optical Society of America

and some rudimentary tensor concepts in the theoretical presentation. A reader who is unfamiliar with tensors may consult any standard textbooks on tensor analysis[17] to pick up the necessary mathematical background.

2. COORDINATE SYSTEMS AND NOTATION

A schematic representation of a crossed grating with a rectangular Cartesian coordinate system attached to it is shown in Fig. 1. The x axis is parallel to one of the periodic directions, and the z axis is perpendicular to the grating plane. The grating layer has a thickness h, and its permittivity, $\epsilon(x, y)$, is a piecewise-constant function taking two values, ϵ_a and ϵ_b. The permittivities above and below the grating layer are $\epsilon_{\pm 1}$, respectively. For the sake of simplicity, we assume that $\epsilon(x, y)$ does not depend on z, although z-variant grating profiles can be easily treated by the so-called multilayer approximation. The grating problem is to determine the diffraction efficiencies, and possibly also the polarization, of the propagating orders when the grating is illuminated by a monochromatic electromagnetic plane wave. The propagation direction of the incident plane wave is given by polar angle θ and azimuthal angle φ. Its polarization, assumed to be linear, is specified by angle ψ with respect to the $p-s$ coordinate system. The unit vector $\hat{p}$ is in the plane of incidence and $\hat{s}$ is perpendicular to it, with both being orthogonal to the incident k vector.

Figure 2 shows the top view of a crossed grating. We introduce a nonrectangular coordinate system $Ox^1x^2x^3$ such that the x^1 and x^3 axes are parallel to the x and z axes, respectively, but the x^2 axis is parallel to another periodic direction of the grating. Among the denumerable periodic directions in the Oxy plane we identify the x^1 and x^2 axes with those two directions that have the shortest periods and denote the two periods d_1 and d_2, respectively. The origin of the z axis is assumed to be at the lower boundary of the grating layer. The angle formed by the positive directions of the x^2 and y axes is ζ, $|\zeta| < \pi/2$. The parallelogram marked by dashed and solid lines and the rectangle marked by the dotted–dashed and solid lines are two possible unit cells of the periodic pattern.

The transformation between the two coordinate systems is given by

$$x^1 = x - y \tan \zeta, \qquad x^2 = y \sec \zeta, \qquad x^3 = z. \quad (1)$$

For the nonrectangular coordinate system, the covariant and the contravariant basis vectors[17] are

$$\mathbf{b}_1 = \hat{x}, \qquad \mathbf{b}_2 = \hat{x} \sin \zeta + \hat{y} \cos \zeta, \qquad \mathbf{b}_3 = \hat{z}, \quad (2)$$

$$\mathbf{b}^1 = \hat{x} - \hat{y} \tan \zeta, \qquad \mathbf{b}^2 = \hat{y} \sec \zeta, \qquad \mathbf{b}^3 = \hat{z}, \quad (3)$$

respectively. The two sets of basis vectors obey the reciprocal relation: $\mathbf{b}_\rho \cdot \mathbf{b}^\sigma = \delta_\rho{}^\sigma$, where $\delta_\rho{}^\sigma$ is the Kronecker delta symbol.

The Gaussian system of units and the implicit harmonic time dependence $\exp(-i\omega t)$ are used here. Although all materials are assumed nonmagnetic, because of symmetry considerations μ is not set equal to 1 in the mathematical formulas. The letter a is used to label the three spatial regions $(0, \pm 1)$; Roman letters m, n, etc., to label Fourier coefficients and matrix elements; and Greek letters ρ, σ, etc., for tensor indices. The Fourier coefficient of a function is denoted by the function name with appropriate subscript(s) (however, not every subscripted symbol is a Fourier coefficient). For a composite function we use notation $(\cdot)_m$ to denote its Fourier coefficient.

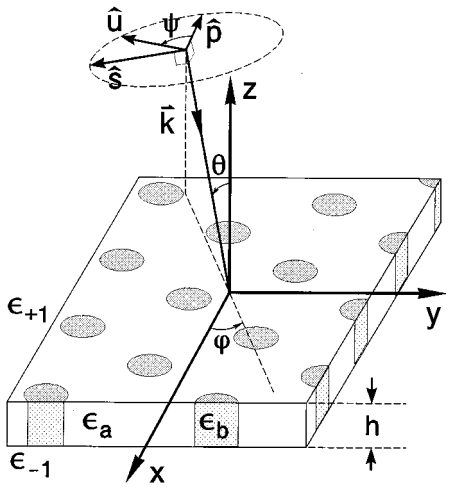

Fig. 1. Crossed grating illuminated by a plane wave. A rectangular Cartesian coordinate system is attached to the grating so that its x axis is along one of the periodic directions.

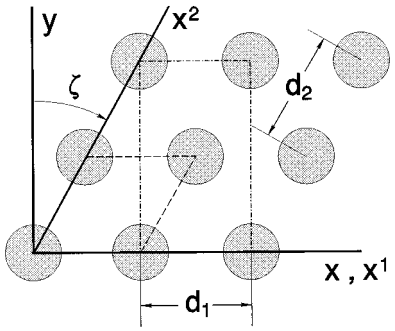

Fig. 2. Top view of a crossed grating and a nonrectangular Cartesian coordinate system in the grating plane. The x^1 and x^2 axes are parallel to two periodic directions of the grating. The x^1 axis is parallel to the x axis, and the x^2 axis forms an angle ζ with the y axis.

In Section 4 the permittivity function $\epsilon(x^1, x^2)$ in the grating layer will be expanded in Fourier series, and several matrices will be subsequently generated. In order to keep the flow of presentation there smooth, some unconventional notations for these matrices will be defined here. The two-dimensional Fourier coefficients of $\epsilon(x^1, x^2)$ are given by

$$\epsilon_{mn} = \frac{1}{d_1 d_2} \int_0^{d_2} \int_0^{d_1} \epsilon(x^1, x^2) \times \exp[-i(mK_1 x^1 + nK_2 x^2)] dx^1 dx^2, \quad (4)$$

where $K_1 = 2\pi/d_1$ and $K_2 = 2\pi/d_2$. These coefficients can be turned into a matrix by splitting the indexing numbers. Introducing the notation $[\![\cdot]\!]$, we have

$$[\![\epsilon]\!]_{mn,jl} = \epsilon_{m-j,n-l}. \tag{5}$$

Next we introduce the notations $[\cdot]$ and $\lfloor\cdot\rfloor$ by

$$[\epsilon]_{mn} = \frac{1}{d_1}\int_0^{d_1} \epsilon(x^1, x^2)\exp[-i(m-n)K_1x^1]\mathrm{d}x^1, \tag{6}$$

$$\lfloor\epsilon\rfloor_{mn} = \frac{1}{d_2}\int_0^{d_2} \epsilon(x^1, x^2)\exp[-i(m-n)K_2x^2]\mathrm{d}x^2. \tag{7}$$

Obviously $[\epsilon]$ and $\lfloor\epsilon\rfloor$ are still functions of x^2 and x^1, respectively. Finally, we introduce two more notations, $[\![\cdot]\!]$ and $\lfloor\!\lfloor\cdot\rfloor\!\rfloor$, by

$$[\![\epsilon]\!]_{mn,jl} = \lfloor\{[1/\epsilon]^{-1}\}_{mj}\rfloor_{nl} = \frac{1}{d_2}\int_0^{d_2}\{[1/\epsilon]^{-1}\}_{mj}(x^2) \times \exp[-i(n-l)K_2x^2]\mathrm{d}x^2, \tag{8}$$

$$\lfloor\!\lfloor\epsilon\rfloor\!\rfloor_{mn,jl} = [\{\lfloor 1/\epsilon\rfloor^{-1}\}_{nl}]_{mj} = \frac{1}{d_1}\int_0^{d_1}\{\lfloor 1/\epsilon\rfloor^{-1}\}_{nl}(x^1) \times \exp[-i(m-j)K_1x^1]\mathrm{d}x^1. \tag{9}$$

In the above, we have assumed that $\epsilon(x^1, x^2) \neq 0$ and the two inverse matrices exist, which is guaranteed on physical grounds.

3. RAYLEIGH SOLUTIONS IN THE HOMOGENEOUS REGIONS

In terms of contravariant basis vectors the wave vector of the incident plane wave may be written as

$$\mathbf{k} = k_\sigma\mathbf{b}^\sigma = \alpha_0\mathbf{b}^1 + \beta_0\mathbf{b}^2 - \gamma_{00}^{(+1)}\mathbf{b}^3, \tag{10}$$

where

$$\alpha_0 = k^{(+1)}\sin\theta\cos\varphi,$$
$$\beta_0 = k^{(+1)}\sin\theta\sin(\varphi+\zeta),$$
$$\gamma_{00}^{(+1)} = k^{(+1)}\cos\theta, \tag{11}$$

$k^{(+1)} = 2\pi\sqrt{[\epsilon^{(+1)}\mu]}/\lambda$, and λ is the vacuum wavelength. $k^{(-1)}$ will be similarly defined. The covariant components of the electric field vectors in regions ±1 can be represented by Rayleigh expansions:

$$E_\sigma(\mathbf{r}) = I_\sigma\exp[i(\alpha_0x^1 + \beta_0x^2 - \gamma_{00}^{(+1)}x^3)] + \sum_{m,n}R_{\sigma mn} \times \exp[i(\alpha_mx^1 + \beta_nx^2 + \gamma_{mn}^{(+1)}x^3)], \quad (x^3 > h), \tag{12}$$

$$E_\sigma(\mathbf{r}) = \sum_{m,n}T_{\sigma mn}\exp[i(\alpha_mx^1 + \beta_nx^2 - \gamma_{mn}^{(-1)}x^3)] \quad (x^3 < 0), \tag{13}$$

where I_σ, $R_{\sigma mn}$, and $T_{\sigma mn}$ are the incident and diffracted field amplitudes,

$$\alpha_m = \alpha_0 + mK_1, \qquad \beta_n = \beta_0 + nK_2, \tag{14}$$

and $\gamma_{mn}^{(a)}$ is to be solved from

$$\sec^2\zeta\,(\alpha_m{}^2 + \beta_n{}^2 - 2\alpha_m\beta_n\sin\zeta) + \gamma_{mn}^{(a)2} = k^{(a)2} \quad (a = \pm1). \tag{15}$$

The sign of $\gamma_{mn}^{(a)}$ should be chosen so that

$$\mathrm{Re}[\gamma_{mn}^{(a)}] + \mathrm{Im}[\gamma_{mn}^{(a)}] > 0 \qquad (a = \pm1). \tag{16}$$

The coefficients α_m, β_n, and $\gamma_{mn}^{(a)}$ are the covariant components of the wave vector of the (m, n)th diffracted order in medium a,

$$\mathbf{k}_{mn}^{(\pm1)} = \alpha_m\mathbf{b}^1 + \beta_n\mathbf{b}^2 \pm \gamma_{mn}^{(\pm1)}\mathbf{b}^3. \tag{17}$$

The projection of tips of the above two k vectors onto the Ox^1x^2 plane for all possible m and n forms the reciprocal lattice of the diffraction orders. In Fig. 3, each intersection point of the dotted lines corresponds to a diffraction order. The cross marks the origin of the space that contains the reciprocal lattice (the k space), and the black dot marks the location of the (0, 0)th order. The lattice constants along directions $\mathbf{b}^1$ and $\mathbf{b}^2$ are $K_1\sec\zeta$ and $K_2\sec\zeta$, respectively. Each smallest parallelogram formed by the dotted lines is a unit cell of the reciprocal lattice.

The set of propagating orders in medium a is given by

$$U^{(a)} = \{(m, n)|\mathrm{Im}[\gamma_{mn}^{(a)}] = 0, \forall m, \forall n\}. \tag{18}$$

Graphically, $U^{(a)}$ is represented by the lattice points that fall within the solid circle in Fig. 3, whose radius is $k^{(a)}$. It is easy to verify that, when $d_1d_2/\lambda^2 \gg 1$, the number of elements in set $U^{(a)}$ is approximately given by

$$\left[\frac{\pi k^{(a)2}}{(K_1K_2/\cos\zeta)}\right] = \left[\frac{\pi(d_1d_2\cos\zeta)}{\lambda^2/(\epsilon^{(a)}\mu)}\right], \tag{19}$$

where $[\cdot]$ means "the integral part of." Thus the number of propagating orders is proportional to the area of the unit cell in real space and inversely proportional to that in the k space.

We now pause to address one of the advantages of being able to use a nonrectangular coordinate system. In

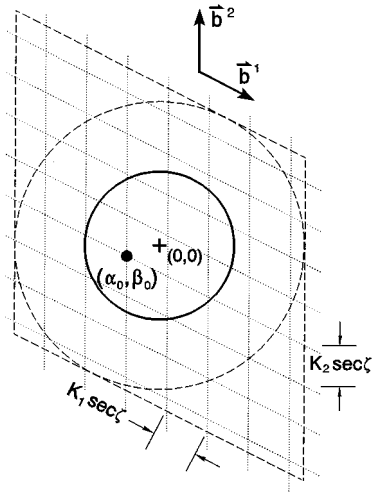

Fig. 3. Section of the reciprocal lattice. The diffraction orders are located at crossings of the grid lines, which are parallel to the contravariant basis vectors. The solid circle indicates the disk of propagating orders. The dashed circle and parallelogram show two truncation schemes.

FMM the dimension of the truncated matrix for numerical computation is essentially the number of lattice points that fall within an area in the reciprocal lattice that contains the disk of propagating orders. Since the density of lattice points in k space is proportional to the area of the unit cell in real space, we should choose one of the smallest unit cells in order to minimize the matrix dimension. If a larger unit cell is chosen, then some of the lattice points will correspond to diffraction orders whose amplitudes are identically zero. This point was clearly recognized by the authors of Ref. 10. However, when they analyzed a periodic pattern as sketched in Fig. 2, they were forced to use the rectangular unit cell, because their formulation was based on a rectangular coordinate system. By using the parallelogramic unit cell, one can reduce the matrix dimension and the computation time by a factor of 2 and 8, respectively, because the area of the parallelogramic unit cell is half that of the rectangular one.

This section concludes with the formula for calculating diffraction efficiencies. If the incident plane wave is normalized such that

$$\frac{1}{\gamma_{00}^{(+1)}}\left[(k^{(+1)2}-\beta_0{}^2)|I_1|^2+(k^{(+1)2}-\alpha_0{}^2)|I_2|^2 + (\alpha_0\beta_0-k^{(+1)2}\sin\zeta)(I_1\overline{I_2}+I_2\overline{I_1})\right]=1, \quad (20)$$

then the (m, n)th-order diffraction efficiency in medium a is given by

$$\eta_{mn}^{(a)}=\frac{1}{\gamma_{mn}^{(a)}}\left[(k^{(a)2}-\beta_n{}^2)|E_{1mn}^{(a)}|^2+(k^{(a)2}-\alpha_m{}^2)|E_{2mn}^{(a)}|^2 + (\alpha_m\beta_n-k^{(a)2}\sin\zeta) \times (E_{1mn}^{(a)}\overline{E_{2mn}^{(a)}}+E_{2mn}^{(a)}\overline{E_{1mn}^{(a)}})\right], \quad (21)$$

where $E_{\sigma mn}^{(+1)}=R_{\sigma mn}$ and $E_{\sigma mn}^{(-1)}=T_{\sigma mn}$.

4. MODAL SOLUTION IN THE GRATING LAYER

In the grating layer the electromagnetic field can be expanded into Floquet–Fourier series,

$$\Psi(x^1, x^2, x^3)=\sum_{m,n}\Psi_{mn}(x^3)\exp(i\alpha_m x^1+i\beta_n x^2), \quad (22)$$

where Ψ stands for any one of the six components of the electric and magnetic vectors. The x^3-dependent Fourier coefficients Ψ_{mn} are to be solved from Maxwell's equations, which in the nonrectangular Cartesian coordinate system take the form[17]

$$\partial_2E_3-\partial_3E_2=ik_0\mu\sec\zeta\,(H_1-\sin\zeta\,H_2), \quad (23a)$$

$$\partial_3E_1-\partial_1E_3=ik_0\mu\sec\zeta\,(H_2-\sin\zeta\,H_1), \quad (23b)$$

$$\partial_1E_2-\partial_2E_1=ik_0\mu\cos\zeta\,H_3, \quad (23c)$$

$$\partial_2H_3-\partial_3H_2=-ik_0\sec\zeta\,\epsilon(E_1-\sin\zeta\,E_2), \quad (24a)$$

$$\partial_3H_1-\partial_1H_3=-ik_0\sec\zeta\,\epsilon(E_2-\sin\zeta\,E_1), \quad (24b)$$

$$\partial_1H_2-\partial_2H_1=-ik_0\cos\zeta\,\epsilon E_3. \quad (24c)$$

To derive the matrix eigenvalue problem we follow closely the steps taken by the authors of Ref. 10. However, in contrast to the case of a lamellar grating, the Fourier analysis of Maxwell's equations with a two-dimensionally varying discontinuous permittivity function is much more complicated. Some preparations are in order here.

In anticipation of applying the Fourier factorization rules of Ref. 14, we first discretize the discontinuity boundary of the permittivity function. Imagine that the plane Ox^1x^2 is covered by a grid whose lines are parallel to the coordinate axes and whose spacings are Δx^1 and Δx^2. Then, as can be seen in Fig. 4, the original contour Γ of the permittivity discontinuity can be approximated by the zigzag contour Γ' which consists of segments of the grid lines. As $\Delta x^1\to 0$ and $\Delta x^2\to 0$, Γ' tends to Γ, and the two contours' optical effects in the far field are indistinguishable for a given wavelength.[18]

Next, we must identify the continuity characteristics of the field components across the boundary Γ'. Since the materials are assumed to be nonmagnetic, all components of the magnetic field vector are continuous. E_3 is also continuous because the grating layer (or each of its sublayers, if a multilayer approximation is used) is z invariant. Let $x_0{}^1$ and $x_0{}^2$ be the locations of some line segments of Γ'. Then away from the vertices of the zigzag contour[18] we have

$$E_1(x_0{}^2+0)=E_1(x_0{}^2-0),$$

$$E_2(x_0{}^1+0)=E_2(x_0{}^1-0), \quad (25)$$

$$\epsilon(x_0{}^1+0)E^1(x_0{}^1+0)=\epsilon(x_0{}^1-0)E^1(x_0{}^1-0), \quad (26a)$$

$$\epsilon(x_0{}^2+0)E^2(x_0{}^2+0)=\epsilon(x_0{}^2-0)E^2(x_0{}^2-0), \quad (26b)$$

where E^1 and E^2 are the contravariant components of the electric field, and for simplicity we have suppressed the irrelevant spatial dependence of the field and permittivity. Equations (25) and (26) are simply the boundary conditions for the electric and electric displacement vectors. To appreciate the beauty of these equations, one has to keep in mind the basic property of vector components in tensor theory: the covariant (contravariant)

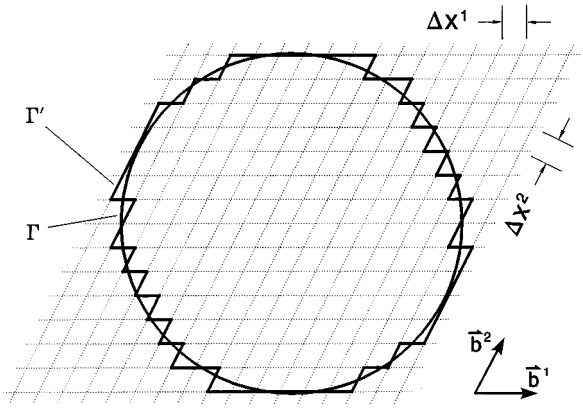

Fig. 4. Discretization of an arbitrary (in this case, a circular) grating contour Γ by a zigzag contour Γ' that consists of line segments of the grid lines parallel to the covariant basis vectors.

components of a vector are the perpendicular projections along the covariant (contravariant) basis vectors, measured in the lengths of the respective basis vectors.

We are now ready to Fourier analyze Eqs. (23) and (24). The reader who is not familiar with the factorization rules to be used below is advised to consult Ref. 14. All three equations in Eqs. (23) and Eq. (24c) can be readily transformed into the Fourier domain by Laurent's rule because they do not contain any product of discontinuous functions. Eliminating E_3, we immediately have

$$\cos\zeta\,\frac{k_0}{i}\,\partial_3 E_{1mn} = +k_0{}^2\mu(H_{2mn} - H_{1mn}\sin\zeta) - \alpha_m\sum_{j,l}[\![\epsilon]\!]^{-1}_{mn,jl}(\alpha_j H_{2jl} - \beta_l H_{1jl}), \tag{27a}$$

$$\cos\zeta\,\frac{k_0}{i}\,\partial_3 E_{2mn} = -k_0{}^2\mu(H_{1mn} - H_{2mn}\sin\zeta) - \beta_n\sum_{j,l}[\![\epsilon]\!]^{-1}_{mn,jl}(\alpha_j H_{2jl} - \beta_l H_{1jl}). \tag{27b}$$

The Fourier analysis of Eqs. (24a) and (24b) however is much more complicated. Let us consider Eq. (24a) first. It can be easily shown that

$$E^1 = \sec^2\zeta\,(E_1 - E_2\sin\zeta) = E_1 - E^2\sin\zeta. \tag{28}$$

Since ϵE^1 is continuous with respect to x^1, the Fourier analysis of Eq. (24a) with respect to x^1 can be accomplished by using the inverse rule. Thus,

$$\frac{\partial_2 H_{3m} - \partial_3 H_{2m}}{ik_0\cos\zeta} + \sum_j\left[\!\!\left[\frac{1}{\epsilon}\right]\!\!\right]^{-1}_{mj}E_{1j} = \sin\zeta\sum_j\left[\!\!\left[\frac{1}{\epsilon}\right]\!\!\right]^{-1}_{mj}E_j{}^2. \tag{29}$$

Since E_1 is continuous in x^2, each of its Fourier coefficients with respect to x^1 is also continuous in x^2. Therefore, each term under the summation sign in the second term on the left-hand side of Eq. (29) can be Fourier factorized with respect to x^2 by Laurent's rule. In order to complete the Fourier analysis, we do the following:

Hypothesis[19]: For every m, the sum on the right-hand side of Eq. (29), i.e., $\Sigma_j[1/\epsilon]^{-1}_{mj}E_j{}^2(x^2)$, is continuous in x^2.

Note that if $\zeta = 0$ this hypothesis is not needed, anyway. Assuming that the hypothesis is true, then the entire left-hand side of Eq. (29) is also continuous in x^2. Multiplying the equation by matrix $[1/\epsilon]$, taking the Fourier coefficients of the result with respect to x^2, and applying Laurent's rule to the left hand side, we get

$$\sum_{j,l}\left[\!\!\left[\frac{1}{\epsilon}\right]\!\!\right]_{mn,jl}\left(\frac{\partial_2 H_{3jl} - \partial_3 H_{2jl}}{ik_0\cos\zeta} + \sum_{s,p}[\![\epsilon]\!]_{jl,sp}E_{1sp}\right) = \sin\zeta\,E^2_{mn}. \tag{30}$$

Using Eq. (23c) to eliminate H_3, we finally have

$$\cos\zeta\,\frac{\mu k_0}{i}\,\partial_3 H_{2mn} = \beta_n(\alpha_m E_{2mn} - \beta_n E_{1mn}) - \mu k_0{}^2\sin\zeta\sum_{j,l}\left[\!\!\left[\frac{1}{\epsilon}\right]\!\!\right]^{-1}_{mn,jl}E_{2jl} + \mu k_0{}^2\sum_{j,l}\left(\cos^2\zeta\,[\![\epsilon]\!]_{mn,jl} + \sin^2\zeta\left[\!\!\left[\frac{1}{\epsilon}\right]\!\!\right]^{-1}_{mn,jl}\right)E_{1jl}. \tag{31a}$$

Following the same procedure, from Eq. (24b) we have

$$\cos\zeta\,\frac{\mu k_0}{i}\,\partial_3 H_{1mn} = \alpha_m(\alpha_m E_{2mn} - \beta_n E_{1mn}) + \mu k_0{}^2\sin\zeta\sum_{j,l}\left[\!\!\left[\frac{1}{\epsilon}\right]\!\!\right]^{-1}_{mn,jl}E_{1jl} - \mu k_0{}^2\sum_{j,l}\left(\cos^2\zeta\,[\![\epsilon]\!]_{mn,jl} + \sin^2\zeta\left[\!\!\left[\frac{1}{\epsilon}\right]\!\!\right]^{-1}_{mn,jl}\right)E_{2jl}. \tag{31b}$$

Eqs. (27) and (31) can be cast in a compact matrix form

$$\cos\zeta\,\frac{k_0}{i}\,\partial_3\begin{pmatrix}E_1\\E_2\end{pmatrix} = F\begin{pmatrix}H_1\\H_2\end{pmatrix},$$

$$\cos\zeta\,\frac{k_0}{i}\,\partial_3\begin{pmatrix}H_1\\H_2\end{pmatrix} = G\begin{pmatrix}E_1\\E_2\end{pmatrix}, \tag{32}$$

with

$$F = \begin{bmatrix}\alpha[\![\epsilon]\!]^{-1}\beta - \mu k_0{}^2\sin\zeta & \mu k_0{}^2 - \alpha[\![\epsilon]\!]^{-1}\alpha\\ \beta[\![\epsilon]\!]^{-1}\beta - \mu k_0{}^2 & \mu k_0{}^2\sin\zeta - \beta[\![\epsilon]\!]^{-1}\alpha\end{bmatrix}, \tag{33}$$

$$G = \begin{bmatrix}\mu k_0{}^2\sin\zeta\left[\!\!\left[\frac{1}{\epsilon}\right]\!\!\right]^{-1} - \alpha\beta & \alpha^2 - \mu k_0{}^2\left(\cos^2\zeta\,[\![\epsilon]\!] + \sin^2\zeta\left[\!\!\left[\frac{1}{\epsilon}\right]\!\!\right]^{-1}\right)\\ \mu k_0{}^2\left(\cos^2\zeta\,[\![\epsilon]\!] + \sin^2\zeta\left[\!\!\left[\frac{1}{\epsilon}\right]\!\!\right]^{-1}\right) - \beta^2 & \alpha\beta - \mu k_0{}^2\sin\zeta\left[\!\!\left[\frac{1}{\epsilon}\right]\!\!\right]^{-1}\end{bmatrix}. \tag{34}$$

In the above, α and β are the short-hand notations for $(\alpha)_{mn,jl} = \alpha_m\delta_{mj}\delta_{nl}$ and $(\beta)_{mn,jl} = \beta_n\delta_{mj}\delta_{nl}$. Equations (33) and (34) can be compared with Eqs. (A9) and (A10) of Ref. 10.

Assuming that a particular solution of Eqs. (32) is proportional to $\exp(i\gamma x^3)$, from these two equations we obtain an algebraic eigenvalue equation

$$(FG - \mu k_0{}^2 \cos^2\zeta\ \gamma^2)\begin{pmatrix} E_1 \\ E_2 \end{pmatrix} = 0. \tag{35}$$

Once the eigenvalues and the electric part of the eigenvectors are found from Eq. (35), the magnetic part of the eigenvectors is given by

$$\begin{pmatrix} H_1 \\ H_2 \end{pmatrix} = \frac{\sec\zeta}{\mu k_0 \gamma} G \begin{pmatrix} E_1 \\ E_2 \end{pmatrix}. \tag{36}$$

Here we exclude the possibility that $\gamma = 0$. From Eq. (35), the eigenvalues come in pairs; if γ is an eigenvalue, so is $-\gamma$. We will only label, with subscript q, the eigensolutions for which

$$\mathrm{Re}[\gamma] + \mathrm{Im}[\gamma] > 0. \tag{37}$$

The modal expansions of the total field in the grating layer can now be written as

$$E_\sigma(\mathbf{r}) = \sum_{m,n,q} [u_q \exp(i\gamma_q x^3) + d_q \exp(-i\gamma_q x^3)] \times \exp[i(\alpha_m x^1 + \beta_n x^2)] E_{\sigma mnq}, \tag{38a}$$

$$H_\sigma(\mathbf{r}) = \sum_{m,n,q} [u_q \exp(i\gamma_q x^3) - d_q \exp(-i\gamma_q x^3)] \times \exp[i(\alpha_m x^1 + \beta_n x^2)] H_{\sigma mnq}, \tag{38b}$$

where $\sigma = 1, 2$, and u_q and d_q are the unknown amplitudes of the upward and downward propagating or decaying modal fields. If the grating region is approximated by several thin layers, then the field expressions in Eqs. (38) are valid for each layer.

5. *S*-MATRIX SOLUTION

Having obtained the expressions of the field everywhere, what remains is to match the boundary conditions at the interfaces between different spatial regions and possibly also at the interfaces, if any, between different sublayers in the grating layer. The result of this operation is a large system of linear equations with the field amplitudes as unknowns. There are many ways to solve this linear system. For best numerical stability and to conserve computer memory, I used the S-matrix algorithm.[20]

In Ref. 20, several systematic and algorithmic procedures, including the S-matrix algorithm, are given for solving the large linear system to obtain the final quantities of interest, namely, the amplitudes $R_{\sigma mn}$ and $T_{\sigma mn}$. To apply these algorithms all we need is to express the Fourier coefficients of the tangential components of the total fields in terms of the unknown field amplitudes. From Eqs. (38), it is easy to see that in a grating layer,

$$\begin{pmatrix} E_{1mn} \\ E_{2mn} \\ H_{1mn} \\ H_{2mn} \end{pmatrix} = \begin{bmatrix} E_{1mnq} & E_{1mnq} \\ E_{2mnq} & E_{2mnq} \\ H_{1mnq} & -H_{1mnq} \\ H_{2mnq} & -H_{2mnq} \end{bmatrix} \times \begin{bmatrix} \exp(i\gamma_q x^3) & 0 \\ 0 & \exp(-i\gamma_q x^3) \end{bmatrix} \begin{pmatrix} u_q \\ d_q \end{pmatrix}. \tag{39}$$

In the above equation, each matrix element symbolizes a rectangular block matrix. For example, E_{1mnq} represents a matrix whose leading dimension runs through all m and n and whose trailing dimension runs through all q. In accordance with the notation of Ref. 20, Eq. (39) can be put in a compact generic form:

$$\Phi = W\phi \begin{pmatrix} \mathbf{u} \\ \mathbf{d} \end{pmatrix}. \tag{40}$$

The Fourier coefficients of the tangential components of the total fields in the two homogeneous regions can also be put in this form. Once this is done, the rest of the work is almost mechanical; following the S-matrix algorithm, we can readily find the unknown Rayleigh amplitudes. The diffraction efficiencies can then be calculated with Eq. (21).

6. MATRIX TRUNCATION

In a numerical analysis the infinite-dimensional matrices and vectors in the preceding two sections must be truncated. In the context of crossed gratings, truncation means to retain a finite number of points that fall within certain area in the k space. This area should contain the disk of propagating orders that was defined in Section 3 (see Fig. 3), because the propagating orders carry energy. From Eq. (15) it is clear that the decay rate of an evanescent order, which lies outside the disk, equals its distance to the circumference of the disk. To ensure numerical accuracy, the boundary of the truncation area should be put sufficiently far away from the disk. So far all authors of crossed gratings have taken the simple truncation scheme that can be described by two inequalities, $|m| \leqslant M$ and $|n| \leqslant N$ for α_m and β_n, where M and N are integers. Graphically, if we refer to Fig. 3, this corresponds to choosing a parallelogramic area that is centered around the (0, 0)th order and whose sides are parallel to the coordinate lines of the k space. This truncation scheme may be called the zeroth-order-centered parallelogramic truncation. Note that the (0, 0)th order in general does not coincide with origin of the k space, except for the case of normal incidence.

It is difficult to say *a priori* which section of the evanescent orders have more weight than the others in determining the overall accuracy of the numerical results; however, it is safe to say that in general the weight of an order decreases as its distance to the origin increases. For simplicity we call this distance the radius of the order. From this viewpoint, the zeroth-order-centered parallelogramic truncation seems to be inconsistent when the angle of incidence is far from normal, because the benefit of having more orders with large radii on one side of the

origin is destroyed by not having enough orders on the other side. Thus an origin-centered parallelogramic truncation as shown in Fig. 3 is a better choice.

Furthermore, it is reasonable to assume that all diffraction orders of approximately equal radii have more or less the same weight. Another possibility is to use a circular truncation as shown by the dashed circle in Fig. 3. An apparent advantage of circular truncation over parallelogramic truncation is that the former takes fewer diffraction orders. It is elementary to show that the ratio of the area of a circular disk to that of the parallelogram in which the disk is perfectly embedded is $(\pi/4)\cos\zeta$. For $\zeta = 0$, this ratio is translated to savings of $1 - (\pi/4)^2 \approx 38\%$ in computer memory and $1 - (\pi/4)^3 \approx 51\%$ in computation time. However, there is a potential problem. For those diffraction orders adjacent to the part of the circumference of the truncation disk that is tangent to a coordinate line of the k space, there may not be enough spatial harmonics along that coordinate line to approximately satisfy the completeness of the Fourier basis functions, whereas for the parallelogramic truncation there is no such a problem.

7. NUMERICAL EXAMPLES

Based on the theory presented above, a computer program was built. The use of the S-matrix algorithm makes the numerical results automatically satisfy the energy balance theorem, irrespective of the matrix truncation; therefore, the theorem cannot be used as an accuracy check here. On the other hand, the ability of the present theory to use different pairs of periodic directions as coordinate axes provides another self-consistency test, which the program successfully passed. The numerical results obtained from the program compared favorably with the few tabulated results that are available in the present literature. In particular, good results were obtained for the famous pyramid grating that has been used by so many authors.[1,2,4,6,9,11,13] It is needless to add another comparison here. Instead, I consider three other examples and show some convergence curves. The choices of the gratings are arbitrary. The purpose of these examples is to illustrate the improvement of the present FMM over the old one and to compare the effectiveness of the origin-centered parallelogramic and circular truncations. The computer program was written to accommodate both truncation schemes easily and to use both the new and the old FMM. Here the old FMM means replacing $[\![\epsilon]\!]^{-1}$ by $[\![1/\epsilon]\!]$ in Eq. (33) and replacing all three matrices containing ϵ in Eq. (34) by $[\![\epsilon]\!]$. If $\zeta = 0$, it corresponds to using Eqs. (A9) and (A10) of Ref. 10 for matrices F and G.

The Fourier coefficients of various ϵ-dependent functions were computed analytically. This is possible because the ϵ-dependent functions are simple rectangular waves in x^1 and/or x^2. The inverses of $[1/\epsilon]$ and $[1/\epsilon]$, for each x^2 and x^1 (because of the discretization as shown in Fig. 4, there are a finite number of them), respectively, were computed by using Trench's algorithm.[21] On the other hand, the inverses of $[\![\epsilon]\!]$ and $[\![1/\epsilon]\!]$ were computed by using a standard alogirthm for general matrices. My numerical experiments showed that the use of a specialized algorithm that takes advantage of the block-Toeplitz characteristics of these two matrices did not lead to any saving in computation time for the matrix sizes encountered in this research.

Before we go into the numerical examples, however, two important questions must be answered. First, what exactly do we mean when we say that method A converges faster than method B? Let η^* be the exact efficiency value of a diffraction order and η_m be the approximation to η^* that is computed by method m at truncation order N, where $m = \mathrm{A}, \mathrm{B}$. Suppose that $|\eta_m - \eta^*| \sim C_m/N^{r(m)}$ as $N \to \infty$, where $r(m) > 0$. To a mathematician, method A converges faster than method B if $r(\mathrm{A})$ is greater than $r(\mathrm{B})$; she or he is thinking of the convergence *rate*. In practice, however, the rate of convergence may be of secondary importance. Two numerical methods may have the same exponent r but very different constants C. Here we adopt a practical measure. If the above absolute error computed by method A goes, as N increases, below certain threshold sooner than that computed by method B, then we say that method A converges faster than method B.

The second and related question is, What is the practical convergence criterion? In numerical grating analysis, the convergence criterion of the preceding paragraph may not be practical because the exact value η^* is not always available. In the case of lamellar gratings,[22] the classical modal method was used to provide a good approximation

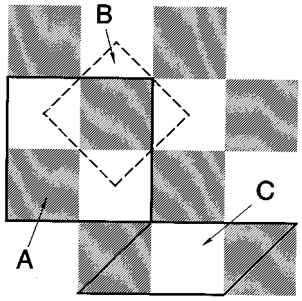

Fig. 5. Top view of the checkerboard grating that is described in Example 1. Areas labeled with letters A, B, and C are three possible unit cells.

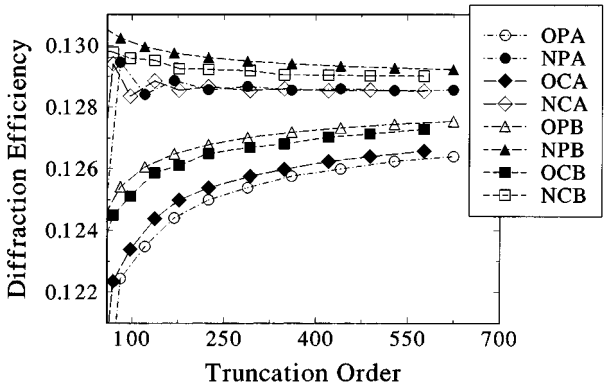

Fig. 6. Convergence of the $(0, -1)$st transmitted order of the checkerboard grating. The letters in the legend have the following denotations: O for old FMM, N for new FMM, P for parallelogramic truncation, C for circular truncation, A for using unit cell A, and B for using unit cell B.

Table 1. Diffraction Efficiencies (%) of the Transmitted Orders of the Checkerboard Grating in Example 1

Diffraction Order	−1	0	+1
−1	4.308	12.860	6.196
0	12.860	17.486	12.860
+1	6.196	12.860	4.308

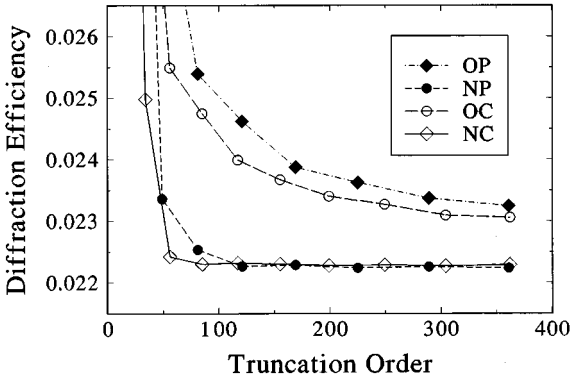

Fig. 7. Convergence of the $(-1, -2)$nd transmitted order of the circular pillar grating in Example 2. The legends read the same way as in Fig. 6.

to η^* in evaluating the convergence of the FMM. Alternatively, one could afford to compute η at an extremely large N and use that as η^*. For crossed gratings, unfortunately, neither an exact modal method nor the option of using an extremely large N is available. Here I am therefore forced to use the flatness of the convergence curves to judge the convergence of various numerical implementations.

A. Example 1

Let us first consider the checkerboard grating that was analyzed by the authors of Ref. 10. A top view of it, along with three possible unit cells labeled A, B, and C, are shown in Fig. 5. The grating parameters are: $\epsilon_{+1} = \epsilon_a = 2.25$, $\epsilon_{-1} = \epsilon_b = 1$, $\theta = \varphi = 0$, $h = \lambda$, the length of each white or black square is 1.25 λ, and the incident polarization is parallel to one side of the squares. In the following, truncation order refers to the total number of diffraction orders retained in the numerical computation. Fig. 6 shows the convergence of the $(0, -1)$st transmitted order (the numbering of the diffraction orders is with reference to the coordinate system that uses the unit cell B). Please note the small increments of the vertical axis. We see several things from this figure: (1) the new FMM converges faster than the old one. (2) The results of using unit cells A and B do not perfectly agree; this is due to the fact that a 1000×1000 grid was used to approximate unit cell B, while no approximation was necessary for unit cell A. However, the difference between the converged results of the new FMM and the old FMM with unit cell B is smaller than that with unit cell A, indicating the advantage of using the smaller unit cell. (3) There is no clear advantage of using circular truncation over parallelogramic truncation. Table 1 gives the diffraction efficiency values of the transmitted orders that were obtained with scheme NPA and truncation order 441. It can be compared with Table 1 of Ref. 10, for which the same truncation order and unit cell were used. In view of Fig. 6, the results given here seem to be more accurate.

B. Example 2

Let us next consider a grating that consists of round pillars arranged to have a hexagonal symmetry, as shown in Fig. 2. The grating parameters are $\epsilon_{+1} = \epsilon_a = 1$, $\epsilon_{-1} = \epsilon_b = 2.56$, $\theta = \varphi = 30°$, $\psi = 0$, $h = \lambda$, $d_1 = d_2 = 2\lambda$, and the pillars have a radius of λ/2. Figure 7 shows the convergence of the $(-1, -2)$nd transmitted order. The parallelogramic unit cell in Fig. 2 was used and the pillar was approximated by a 1000×1000 grid. Once again, the new FMM converges much faster than the old one. In this particular case the circular truncation gives faster convergence than the parallelogramic truncation with the old FMM, but there is no difference with the new FMM. The complete set of diffraction efficiency values for this grating, computed using the NP scheme, 361 diffraction orders, and a 2000×2000 grid, are given in Tables 2 and 3. The positions corresponding to the nonpropagating orders are left blank. For the chosen angle of incidence and polarization, the diffraction efficiencies should have a mirror symmetry with respect to the main diagonal of the table. The slight asymmetry in some of the diffraction order pairs results from the zigzag approximation. As the grid density increases, this asymmetry should diminish.

C. Example 3

So far, to my knowledge, there has not been any published data of metallic crossed gratings computed with the FMM. Figure 8 shows the top view of the metallic

Table 2. Diffraction Efficiencies (%) of the Circular Pillar Grating in Example 2: Reflected Orders

Diffraction Order	−2	−1	0	+1
−2	0.072	0.198	—	—
−1	0.198	0.005	0.361	—
0	—	0.360	0.394	0.209
+1	—	—	0.209	—

Table 3. Diffraction Efficiencies (%) of the Circular Pillar Grating in Example 2: Transmitted Orders

Diffraction Order	−4	−3	−2	−1	0	+1	+2
−4	—	—	0.020	—	—	—	—
−3	—	0.993	1.078	0.829	0.167	—	—
−2	0.020	1.078	1.107	2.224	2.976	0.231	—
−1	—	0.829	2.224	11.127	10.948	1.585	—
0	—	0.167	2.973	10.944	5.929	11.953	0.523
+1	—	—	0.230	1.584	11.961	11.032	1.369
+2	—	—	—	—	0.523	1.370	—

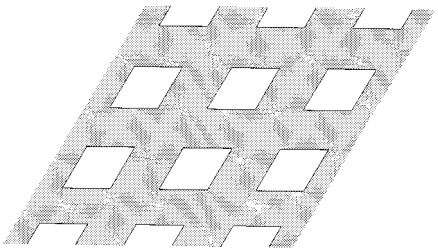

Fig. 8. Top view of the metallic grating that is considered in Example 3.

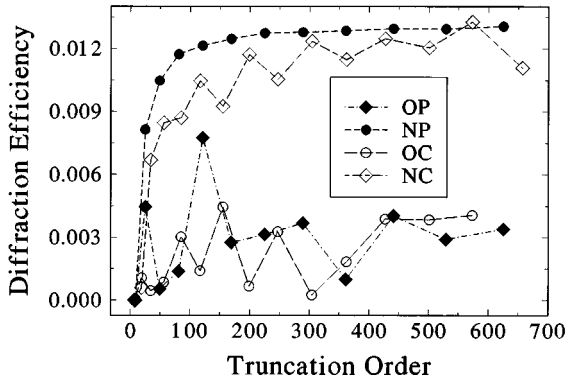

Fig. 9. Convergence of the $(0, -1)$th transmitted order of the metallic grating in Example 3. The legends read the same way as in Figs. 6 and 7.

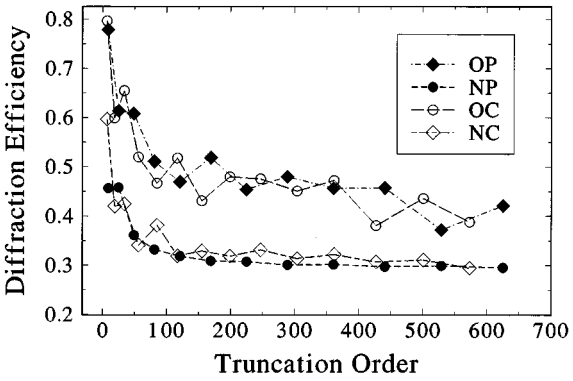

Fig. 10. The same as Fig. 9, but for the $(0, 0)$th reflected order.

grating, which is a metallic grid. The grating parameters are $\epsilon_{+1} = \epsilon_b = 1$, $\epsilon_{-1} = 2.25$, $\epsilon_a = 1.0 + i5.0$, $\theta = \varphi = 30°$, $\psi = 0$, $\zeta = 30°$, $h = \lambda$, $d_1 = d_2 = 2\lambda$, the sides of the parallelogramic holes are parallel to the coordinate axes, and they have an equal length of λ. For this geometry a 1×1 grid suffices. The convergence curves of the $(0, -1)$st transmitted and the $(0, 0)$th reflected orders are shown in Figs. 9 and 10, respectively. The results with the new FMM and parallelogramic truncation converge fairly well. Those with circular truncation do not converge as well, but their tendency to converge is evident. The reader is reminded of the comment that I made at end of Section 6 on the potential problem of circular truncation. In contrast, the results of the old FMM show no sign of converging at all. This is hardly surprising if one recalls how slowly the old FMM converged for metallic lamellar gratings.[21] The complete set of diffraction efficiency values for this grating, computed with the NP scheme and 625 diffraction orders, are given in Tables 4 and 5.

In a numerically oriented theoretical paper such as this, it is desirable to provide some information about computation time. Unfortunately, this information is at present not available. The numerical results of this section are actually a compilation of computations done on four computers of the same manufacturer but of different central processing units and memory sizes. Furthermore, the executable codes were generated on the slowest computer of the four. This fact made the acquisition of accurate timing information impossible. However, it is worthwhile pointing out that the assembly of the four ϵ-related matrices appearing in Eqs. (33) and (34) takes a negligible amount of computation time compared with that needed for solving the eigenvalue problem of Eq. (35).

8. SUMMARY

A new formulation of the FMM that applies the correct rules of Fourier factorization for crossed surface-relief gratings has been presented. Although the work reported here is preliminary, the numerical examples have convincingly shown that the new FMM converges much faster than the old FMM. The new FMM is used to produce well-converged numerical results for metallic crossed gratings. In addition, the new formulation adopts a general nonrectangular Cartesian coordinate system that gives the FMM greater generality and in some cases the ability to save computer memory and computation time. Numerical experiments with parallelogramic and circular truncation schemes indicate that the former is the better choice.

Table 4. Diffraction Efficiencies (%) of the Metallic Grating in Example 3: Reflected Orders

Diffraction Order	−2	−1	0	+1
−2	0.580	0.549	—	—
−1	0.549	2.373	4.627	—
0	—	4.627	29.547	6.238
+1	—	—	6.238	—

Table 5. Diffraction Efficiencies (%) of the Metallic Grating in Example 3: Transmitted Orders

Diffraction Order	−3	−2	−1	0	+1	+2
−3	0.006	0.137	0.249	—	—	—
−2	0.137	0.648	1.150	0.509	—	—
−1	0.249	1.150	1.995	1.307	0.355	—
0	—	0.509	1.307	1.286	0.436	0.075
+1	—	—	0.355	0.436	0.359	0.046
+2	—	—	—	0.075	0.046	—

ACKNOWLEDGMENTS

I am grateful to Eero Noponen of Helsinki University of Technology for providing me some diffraction efficiency data during the program-debugging phase of this work and to Robert L. Kingston and Stuart F. Biggar of the University of Arizona and Bruce W. Shore of Lawrence Livermore National Laboratory for giving me permission to use three computers with large memory, which were used to obtain those data points of Section 7 for which the truncation order is greater than 250.

REFERENCES AND NOTES

1. P. Vincent, "A finite-difference method for dielectric and conducting crossed gratings," Opt. Commun. **26**, 293–296 (1978).
2. D. Maystre and M. Nevière, "Electromagnetic theory of crossed gratings," J. Opt. (Paris) **9**, 301–306 (1978).
3. S. T. Han, Y.-L. Tsao, R. M. Walser, and M. F. Becker, "Electromagnetic scattering of two-dimensional surface-relief dielectric gratings," Appl. Opt. **31**, 2343–2352 (1992).
4. G. H. Derrick, R. C. McPhedran, D. Maystre, and M. Nevière, "Crossed gratings: a theory and its applications," Appl. Phys. **18**, 39–52 (1979).
5. R. C. McPhedran, G. H. Derrick, M. Nevière, and D. Maystre, "Metallic crossed gratings," J. Opt. (Paris) **13**, 209–218 (1982).
6. G. Granet, "Diffraction par des surfaces bipériodiques: résolution en coordonnées non-orthogonales," Pure Appl. Opt. **4**, 777–793 (1995).
7. J. B. Harris, T. W. Preist, J. R. Sambles, R. N. Thorpe, and R. A. Watts, "Optical response of bigratings," J. Opt. Soc. Am. A **13**, 2041–2049 (1996).
8. D. C. Dobson and J. A. Cox, "An integral equation method for biperiodic diffraction structures," in *International Conference on the Application and Theory of Periodic Structures*, J. M. Lerner and W. R. McKinney, eds., Proc. SPIE **1545**, 106–113 (1991).
9. R. Bräuer and O. Bryngdahl, "Electromagnetic diffraction analysis of two-dimensional gratings," Opt. Commun. **100**, 1–5 (1993).
10. E. Noponen and J. Turunen, "Eigenmode method for electromagnetic synthesis of diffractive elements with three-dimensional profiles," J. Opt. Soc. Am. A **11**, 2494–2502 (1994).
11. J.-J. Greffet, C. Baylard, and P. Versaevel, "Diffraction of electromagnetic waves by crossed gratings: a series solution," Opt. Lett. **17**, 1740–1742 (1992).
12. O. P. Bruno and F. Reitich, "Numerical solution of diffraction problems: a method of variation of boundaries. III. Doubly periodic gratings," J. Opt. Soc. Am. A **10**, 2551–2562 (1993).
13. O. P. Bruno and F. Reitich, "Calculation of electromagnetic scattering via boundary variations and analytic continuation," Appl. Computat. Electromagn. Soc. J. **11**, 17–31 (1996).
14. L. Li, "Use of Fourier series in the analysis of discontinuous periodic structures," J. Opt. Soc. Am. A **13**, 1870–1876 (1996).
15. P. Lalanne and G. M. Morris, "Highly improved convergence of the coupled-wave method for TM polarization," J. Opt. Soc. Am. A **13**, 779–784 (1996).
16. G. Granet and B. Guizal, "Efficient implementation of the coupled-wave method for metallic lamellar gratings in TM polarization," J. Opt. Soc. Am. A **13**, 1019–1023 (1996).
17. See, for example, R. C. Wrede, *Introduction to Vector and Tensor Analysis* (Dover, New York, 1972), Chap. 1.
18. We ignore the electromagnetic edge effect at the vertices of the zigzag contour. In the far field, this artificially introduced edge effect should be negligible.
19. At the time of the writing, I have not mathematically proven the validity or invalidity of the hypothesis. However, the numerical examples given in Section 7 seem to support this hypothesis. The sum clearly corresponds to the Fourier coefficient of ϵE^2 with respect to x^1, albeit in a complicated way. The latter, as indicated in Eq. (26b), is continuous with respect to x^2.
20. L. Li, "Formulation and comparison of two recursive matrix algorithms for modeling layered diffraction gratings," J. Opt. Soc. Am. A **13**, 1024–1035 (1996).
21. S. Zohar, "Toeplitz matrix inversion: the algorithm of W. F. Trench," J. Assoc. Comput. Mach. **16**, 592–601 (1969).
22. L. Li and C. W. Haggans, "Convergence of the coupled-wave method for metallic lamellar diffraction gratings," J. Opt. Soc. Am. A **10**, 1184–1189 (1993).